AGU PUBLICATIONS

JGR

Journal of Geophysical Research: Space Physics

RESEARCH ARTICLE
10.1002/2017JA024463

Key Points:
- Mars Express heavy ion data outside the magnetic boundary show a statistical asymmetry consistent with other energetic plume studies
- The energetic plume is more prevalent on the dayside (i.e., $X > 0$), while for $X < 0$ higher count rates in the $+E_{SW}$ direction were not seen
- For a specific instrument setting, overlap between proton contamination and the plume is rare, allowing for confident plume identification

Supporting Information:
- Supporting Information S1

Correspondence to:
B. C. Johnson,
blakecjo@umich.edu

Citation:
Johnson, B. C., Liemohn, M. W., Fränz, M., Ramstad, R., Stenberg Wieser, G., & Nilsson, H. (2018). Influence of the interplanetary convective electric field on the distribution of heavy pickup ions around Mars. *Journal of Geophysical Research: Space Physics*, *123*, 473–484. https://doi.org/10.1002/2017JA024463

Received 12 JUN 2017
Accepted 7 DEC 2017
Accepted article online 13 DEC 2017
Published online 24 JAN 2018

Influence of the Interplanetary Convective Electric Field on the Distribution of Heavy Pickup Ions Around Mars

B. C. Johnson[1], M. W. Liemohn[1], M. Fränz[2], R. Ramstad[3], G. Stenberg Wieser[3], and H. Nilsson[3]

[1]Department of Climate and Space Sciences and Engineering, University of Michigan, Ann Arbor, MI, USA, [2]Max-Planck Institute for Solar System Research, Göttingen, Germany, [3]Swedish Institute of Space Physics, Kiruna, Sweden

Abstract This study obtains a statistical representation of 2–15 keV heavy ions outside of the Martian-induced magnetosphere and depicts their organization by the solar wind convective electric field (E_{SW}). The overlap in the lifetime of Mars Global Surveyor (MGS) and Mars Express (MEX) provides a period of nearly three years during which magnetometer data from MGS can be used to estimate the direction of E_{SW} in order to better interpret MEX ion data. In this paper we use MGS estimates of E_{SW} to express MEX ion measurements in Mars-Sun-Electric field (MSE) coordinates. A new methodological technique used in this study is the limitation of the analysis to a particular instrument mode for which the overlap between proton contamination and plume observations is rare. This allows for confident energetic heavy ion identification outside the induced magnetosphere boundary. On the dayside, we observe high count rates of 2–15 keV heavy ions more frequently in the $+E_{SW}$ hemisphere ($+Z_{MSE}$) than in the $-E_{SW}$ hemisphere, but on the nightside the reverse asymmetry was found. The results are consistent with planetary origin ions being picked up by the solar wind convective electric field. Though a field of view hole hinders quantification of plume fluxes and velocity space, this new energetic heavy ion identification technique means that Mars Express should prove useful in expanding the time period available to assess general plume loss variation with drivers.

Plain Language Summary The location and flow direction of oxygen escaping Mars' atmosphere is organized by a global-scale electric field associated with the Sun's flowing magnetic field. While the Mars Express (MEX) satellite is less well equipped than Mars Atmosphere and Volatile Evolution (MAVEN) to estimate exact flux values of ions accelerated by this electric field, our demonstration that MEX can see this population statistically opens a new window of time (pre-MAVEN) to studies of the variability of this atmospheric escape channel.

1. Introduction

The escape of planetary ions from the atmosphere of Mars into space has been investigated using measurements taken by Phobos-2, Mars Express (MEX), and the Mars Atmosphere and Volatile Evolution (MAVEN) spacecraft. Already in the Phobos-2 data there was evidence of a population of energetic heavy planetary ions, known as pickup ions, that extends outside of the induced magnetosphere boundary (IMB) (e.g., Kallio et al., 1995, Lundin & Dubinin, 1992). Energetic planetary ions beyond the IMB were later also observed in MEX data (e.g., Lundin et al., 2008). Analyses of both Phobos-2 and MEX data sets suggested that less energetic ions flowing within or close to the IMB dominated ion escape (e.g., Barabash et al., 2007; Lundin & Dubinin, 1992). Additionally, MEX heavy ion data from the magnetosheath is often contaminated by strong proton fluxes, complicating the process of examining a region already thought to be of minor importance in terms of total escape fluxes (Nilsson et al., 2011). As a consequence, MEX studies of heavy ions have tended to focus on ions located inside of the IMB (e.g., Barabash et al., 1991; Dubinin et al., 1996, 2006; Fedorov et al., 2006; Liemohn et al., 2014; Lundin et al., 2004; Nilsson et al., 2011, 2012).

At the same time, multiple numerical models predicted significant fluxes of pickup ions well outside of the IMB with initial trajectories not downtail, but in the direction of the solar wind convective electric field, $E_{SW} = -v_{SW} \times B_{IMF}$, where IMF stands for interplanetary magnetic field (e.g., Boesswetter et al., 2004; Fang et al., 2008; Harnett & Winglee, 2006; Kallio et al., 2006; Kallio & Koskinen, 1999; Luhmann & Schwingenschuh, 1990; Modolo et al., 2005; Najib et al., 2011). In the $-E_{SW}$ hemisphere—the hemisphere

where the electric field points toward Mars—this ion population was predicted to be accelerated into the atmosphere and lost. In the $+E_{SW}$ hemisphere, however, the ions are expected to be accelerated away from the planet in a direction perpendicular to the bulk solar wind flow, roughly perpendicular to the Sun-Mars line. In some cases, this energetic plume of pickup ions was predicted to contain as much particle flux as the central tail loss channel (Curry et al., 2013; Liemohn et al., 2013). The physics of ion pickup is not unique to Mars. What sets Mars apart is that the gyroradius of solar wind pickup ions at Mars can be large enough to result in planet-scale asymmetries, where 10 keV O^+ (O_2^+) ions flowing perpendicular to an ~10 nT magnetic field have gyroradii of about 1.7 (2.4) Mars radii. The most natural comparison would be Venus, another inner planet with an induced magnetosphere, where proximity to the Sun results in stronger IMF, a more radial parker spiral results in pickup ion velocities that are less perpendicular to the solar wind flow (reducing $v \times B$), and the planet's larger gravity results in fewer ions being born at the exospheric altitudes at where the requisite fast convective plasma flow is located. These three factors do not compete. They all work together to reduce the gyroradius, making planet-scale gyroradii the exception at Venus. At Mars, however, such large-scale asymmetries appear to be the norm.

Asymmetries in the planetary ion flow around Mars related to the effects of crustal fields have been observed previously (e.g., Lundin et al., 2011). Global asymmetries in the distribution of ions around Mars caused specifically by E_{SW} have also been reported, but these studies were either focused exclusively on ions observed within the IMB (Carlsson et al., 2008; Dubinin et al., 2006) or included ions from a broad energy range, allowing the less energetic ions to dominate the results (Barabash et al., 2007; Dubinin et al., 2006; Fedorov et al., 2006, 2008). Pickup ions such as those produced in numerical models—a high energy population that can extend outside the IMB—have also been reported (Dubinin et al., 2011; Edberg et al., 2009; Liemohn et al., 2014). These studies describe ion populations that increase in energy with distance from the planet, consistent with acceleration by E_{SW}, but these were case studies including only a small number of observations. A statistical survey of MEX data for energetic heavy ions outside of the IMB was still absent.

Recently, Brain et al. (2015) reported a strong asymmetry in net ion escape based on the direction of E_{SW}, and Dong et al. (2015) used 3 months of ion measurements from the MAVEN spacecraft's SupraThermal and Thermal Ion Composition (STATIC) instrument and the MAVEN magnetometer upstream of the bow shock to make a limited statistical survey of energetic O^+ in a solar wind electric field oriented coordinate system.

The present paper seeks to corroborate and expand these MAVEN results by using MEX data from the full two and half year stretch during which Mars Global Surveyor (MGS) could be used to estimate the direction of E_{SW}. While case studies of the energetic plume beyond the IMB have been found in the MEX ion data (e.g., Dubinin et al., 2006, 2011; Liemohn et al., 2014), a comprehensive statistical survey has not been undertaken because scattering of solar wind protons within the instrument obscure the heavy ion signature in the data. To conduct a thorough statistical study, a new methodology to isolate energetic heavy ion observations from solar wind proton contamination was implemented, allowing for confident plume identification from the MEX ion data set beyond the IMB. Utilizing time intervals when such estimates of the direction of E_{SW} were determined to be most reliable, we rotate the data into a coordinate system aligned with the convective electric field to investigate how 2–15 keV planetary ions outside the IMB are organized by E_{SW}.

2. Data Sets and Methodology

To explore the role of the convective electric field in organizing heavy ions originating from the Martian upper atmosphere, ion data are combined with magnetic field data. The ion data were detected by the Ion Mass Analyzer (IMA) that is part of the Analyzer of Space Plasma and Energetic Atoms (ASPERA-3) instrument suite aboard MEX. Detailed descriptions of the ASPERA-3 instruments can be found in Barabash et al. (2004, 2006). The direction of the convective electric field was estimated using magnetometer data from MGS.

It takes 192 s for IMA to complete energy sweeps (96 energy steps in the range of 10 eV–32 keV per charge) for 16 different look directions (scanning from −45 to +45° out of the aperture plane). IMA detects ion masses within the range of 1–44 atomic mass unit. The present work only considers ions that are heavy (O^+, O_2^+, and CO_2^+) and in the 2–15 keV energy range. For each 192 s data packet, the count rate and velocity of heavy ions in this energy range was recorded, as was the position of MEX in the Mars-centered Solar Orbital (MSO) coordinate system. This information was matched with an estimate of the upstream IMF direction at that time.

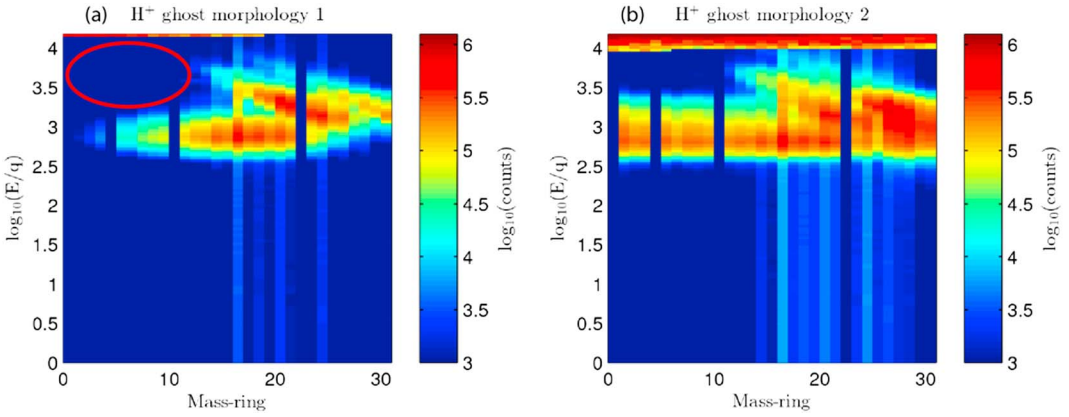

Figure 1. Integrated solar wind measurements showing how solar wind protons are dispersed across IMA's mass channels when IMA is operating in two different modes: (a) a post acceleration of 2,400 V and (b) a post acceleration of 4,200 V. The energy-mass regime from which data were taken for this study is indicated qualitatively with a red oval. The important point is that the oval is empty. This highlights the fact that for the post acceleration voltage for which data were used in this study, we were able to restrict the study to an energy and mass range that is free of ghost count contamination.

Assigning an upstream IMF direction to each data packet required that we limit our search through MEX data to the period of overlap in the lifetime of MEX and MGS. This period extends from early 2004 through autumn 2006. During this time, MGS was in a 2 .a.m.–2 p.m. Sun-synchronous orbit at 400 km altitude with a period of 2 h. At 400 km altitude, the magnetic field configuration around Mars corresponds to a heavily draped IMF (e.g., Brain et al., 2006; Liemohn et al., 2007). Using the assumption that the IMF field lines drape parallel around the planet (remaining in the same plane as the upstream field line), Brain et al. (2006) developed a 2 h cadence data set that provides estimates of the upstream clock angle, $\cup_{IMF}$, using magnetometer data from the 400 km orbit of MGS. This set of IMF clock angle estimates has been widely used (e.g., Carlsson et al., 2008; Dieval et al., 2014; Dubinin et al., 2008; Nilsson et al., 2011; Wang et al., 2013), and we adopt it as the IMF clock angle proxy used in the present work. There is a large uncertainty in this estimation of $\cup_{IMF}$ due to draping configurations that are not ideal and due to time variation in $\cup_{IMF}$. To minimize the uncertainty due to the time variation of $\cup_{IMF}$, we only use ion data from periods when $\cup_{IMF}$ appeared to be steady. More precisely, ion data were included in this survey only if its corresponding $\cup_{IMF}$ value was within 15° of the previous $\cup_{IMF}$ (the estimate from 2 h earlier) and within 15° of the following $\cup_{IMF}$ (from 2 h later). The ion data within ±60 min of the middle "steady" $\cup_{IMF}$ value were included in the survey. We also exclude data from times when MEX was inside the IMB. The most precise way to isolate time intervals outside the IMB would be to identify boundary crossings for each orbit, but given the large quantity of data we chose the more practical method of automatically selecting times when MEX was outside of an average IMB location estimated empirically by Vignes et al. (2000). A histogram of the estimated clock angle of E_{SW} is shown in Figure 2. The clustering of E_{SW} clock angle values around 330° corresponds to the clustering of IMF draping angles around 240° discussed in Brain et al. (2006) and indicates a systematic error in this proxy, which will be brought up again in the discussion. Here we simply ask readers to keep in mind as they view the figures that the site from which we downloaded this draping proxy warns that it is not thought to be more accurate than ~90°. For this reason, our analysis consists of coarse comparisons of Mars-Sun-Electric field (MSE) hemispheres and quadrants (quarter-cylinders) despite the modeled energetic plume often appearing narrowly focused in the direction of *E*.

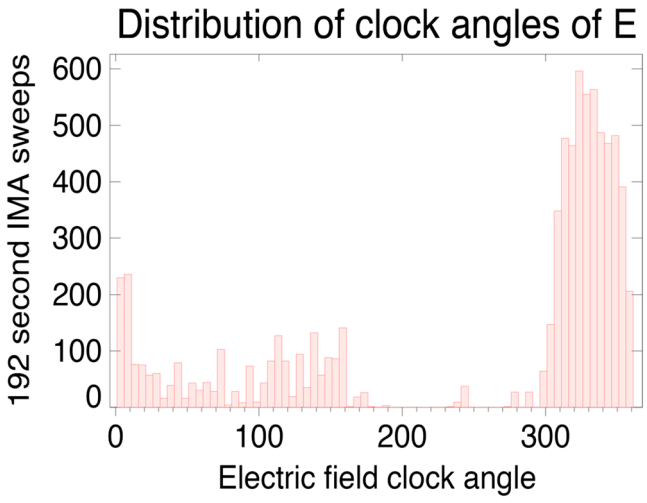

Figure 2. Histogram showing the distribution of clock angles estimated from MGS draping angle proxy. The angle is defined counterclockwise from local east. The large peak at a convective electric field angle of around 330° corresponds to the clustering of IMF draping angles at 240° as discussed in Brain et al. (2006) and explains the asymmetry in data coverage seen here in Figure 3.

One difficulty encountered when studying MEX IMA data outside the IMB is that of cleaning the data to remove H^+ "ghost" counts, which occur when solar wind protons cause false counts in heavy ion mass rings. Ghost counts are false counts that appear when a proton's path inside of IMA misses the

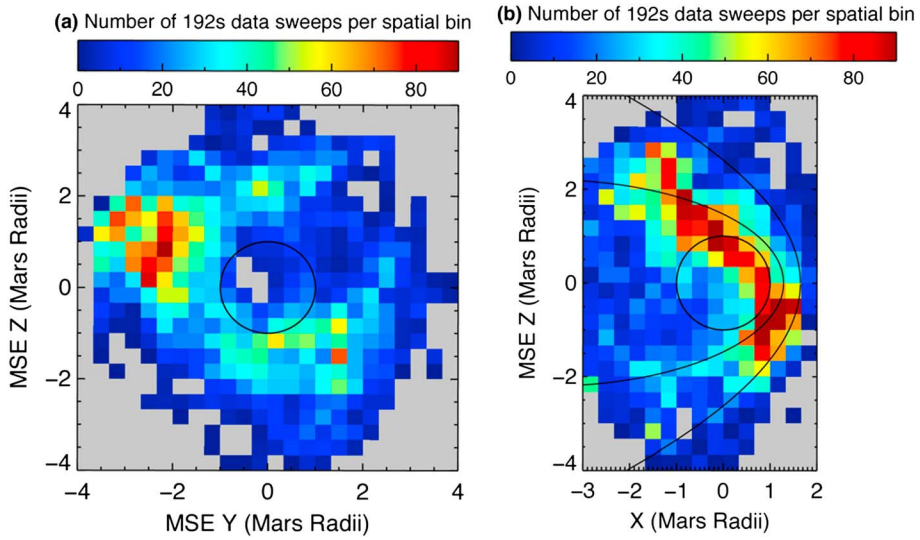

Figure 3. Coverage of the data used in this study in MSE coordinates, with the direction of the convective electric field directed upward along the vertical axis. (a) The *X*-integrated coverage as viewed from the Sun. (b) The *Y*-integrated coverage. The circle represents Mars and the curves are average locations of the bow shock and IMB. The color of each bin indicates how many times that region was sampled.

detector. Figure 1 helps illustrate where such proton contamination occurs as a function of energy and mass ring (an energy-mass matrix). Figure 1a shows many integrated solar wind measurements taken when the post acceleration setting of IMA was 2,400 V, whereas Figure 1b shows a similar integrated energy-mass-matrix, but for a post acceleration setting of 4,200 V. To minimize H^+ contamination of the heavy mass rings, we restrict the study to times when IMA was operating with a post acceleration voltage of 2,400 V, and only include ions striking mass rings 0–11 in the 2–15 keV energy range. This range is loosely indicated by a red oval in Figure 1a. For this energy range and post-acceleration (PAC) setting, protons inside IMA strike the detector well away from the detector's edge, resulting in an order of magnitude reduction in ghost counts, making it unlikely that ghost counts have significantly impacted our findings.

The resulting data set consists of about eight thousand 192 s long ion data packets from times when MEX was outside the model IMB and IMA was switched on and using the 2,400 V post acceleration voltage and the IMF clock angle was steady. In our results, ion locations and flight directions have been transformed into the Mars-

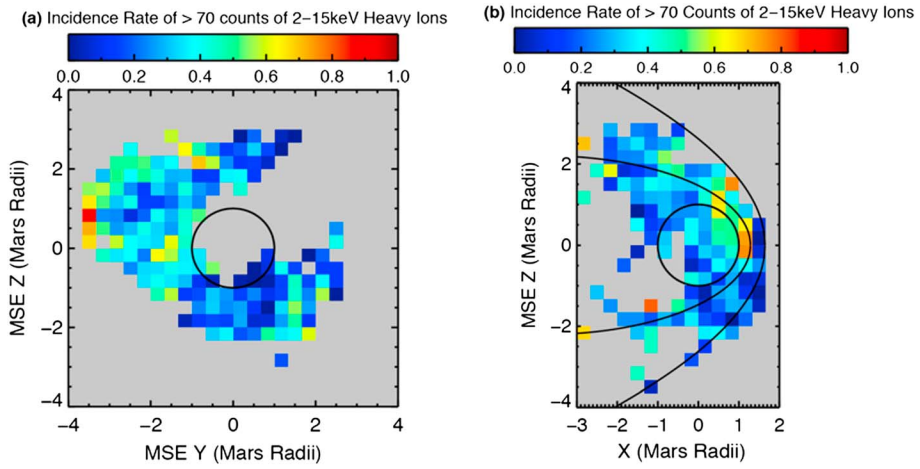

Figure 4. Incidence rate of high counts. (a) Integrated along *X*. (b) Integrated along *Y*. The color of each spatial bin denotes the fraction of the total number of data samples in that bin with a count rate >70. Spatial bins with less than 20 measurements appear in grey.

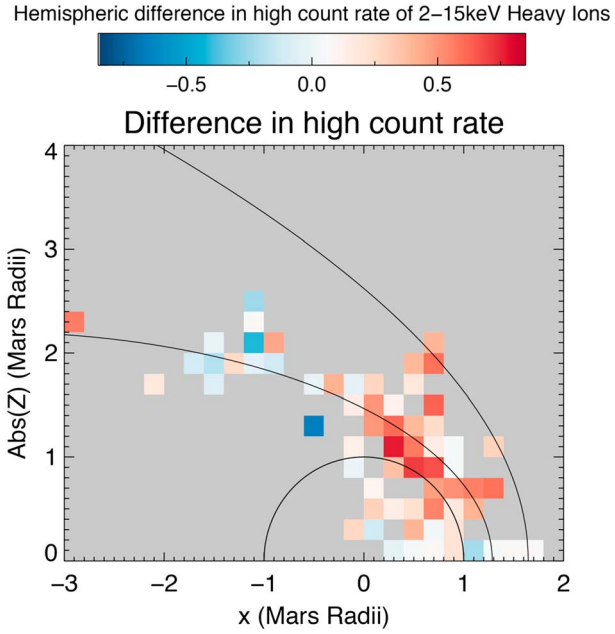

Figure 5. Difference in incidence rate of high counts between the $+E_{SW}$ and $-E_{SW}$ hemispheres. The vertical axis is the absolute value of Z_{MSE}. The color represents the incidence rate of high counts in the $+E_{SW}$ direction minus the incidence rate of high counts in the corresponding spatial bin in the $-E_{SW}$ direction. Spatial bins for which there were not at least 10 samples of data from the $+E_{SW}$ hemisphere and at least 10 samples of data from the $-E_{SW}$ hemisphere appear in grey. Data have been integrated along Y prior to calculating the difference.

Sun-Electric field (MSE) coordinate system by rotating around the MSO x axis until the z axis was parallel to the direction of the convective electric field.

A map of the data coverage around Mars in MSE coordinates is shown in Figure 3. The circle represents the planet, and the curves in Figure 3b represent average locations of the IMB and bow shock as estimated by Vignes et al. (2000). Figure 3a shows the view from the Sun, integrating over all X for which there was data available, with Y_{MSE} on the horizontal axis and Z_{MSE} on the vertical axis. This panel highlights the fact that not all clock angles of the IMF are evenly sampled. MEX was most often in the $-Y_{MSE}$ and $+Z_{MSE}$ hemispheres. In principle, this uneven sampling in MSE coordinates should not occur, as Mars is expected to spend a roughly equal amount of time in the toward and away sectors of the solar wind over the course of two and a half years. The sampling asymmetry is explained by the distribution of the E_{SW} proxy shown in Figure 2. Due to the large clustering of E_{SW} values, transformation into the MSE system rotates but partially preserves the MSO clustering of MEX's position during this time. Figure 3b shows the X-Z_{MSE}-plane, where we have integrated over Y_{MSE} from −4 to +4 Mars radii. Note that values appear "inside" of the projection. All measurements included in this study are outside of the Vignes et al. (2000) IMB location. It should be noted that most of the data taken in the $-E_{SW}$ hemisphere are on the dayside, whereas in the $+E_{SW}$ hemisphere, the region most heavily sampled is slightly downtail of the $X = 0$ plane. Therefore, if we used only a view from the Sun projected onto a plane, it would be difficult to determine whether differences seen between the $+E_{SW}$ and $-E_{SW}$ hemispheres are actually due to asymmetries caused by the direction of E_{SW} or whether such differences are due data from these separate hemispheres being dominated by different regions along the Mars-Sun line. For this reason, some separate analyses have been performed for dayside and for nightside.

3. Results

Figure 4 is a map of the incidence rate (occurrence frequency) of significant counts of 2–15 keV heavy ions. By "high counts" here, we mean values above 70. As will be discussed below, a count rate of 70 or more is an indication that a physically meaningful presence of heavy ions was observed by MEX IMA, above any background level of noise count rate. The incidence rate of the high count observations is a value from 0 to 1, with values approaching 1 indicating that a significant number of heavy ions are observed on nearly every 192 s data packet. For example, an incidence rate of 0.6 means that for 60% of all 192 s data packets in that spatial bin, the integrated counts of heavy ions across all instruments that look directions within the 2–15 keV energy range were at least 70. For statistical significance, we have also limited the values shown in Figure 4 to only those spatial bins with more than 20 MEX IMA data packets. These maps use the same MSE coordinate system used in Figure 3, with (a) showing the view from the Sun and (b) showing the X-Z_{MSE}-plane.

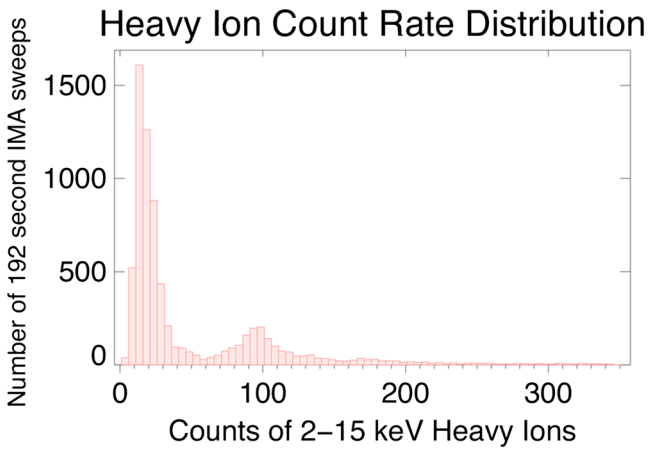

Figure 6. This histogram shows the number of IMA data packets (vertical axis) that detected a given number of counts of 2–15 keV heavy ions (horizontal axis). For most data packets, the count rate was between 10 and 50. A count rate greater than 70 is considered to be "high counts" for the purposes of this study.

Figure 4a does not seem show a clear trend of there being increased count rates of energetic heavy ions in the $+E_{SW}$ direction. It does indicate, however, that it is rare to see large numbers of these ions in the $-E_{SW}$ direction. Figure 4b reveals that if we integrate over all Y_{MSE}, it becomes clear that on the dayside, the $+E_{SW}$ hemisphere has a far greater incidence rate of high counts than the $-E_{SW}$ hemisphere. To ease comparison between the hemispheres, Figure 5 shows the difference between the incidence rate in

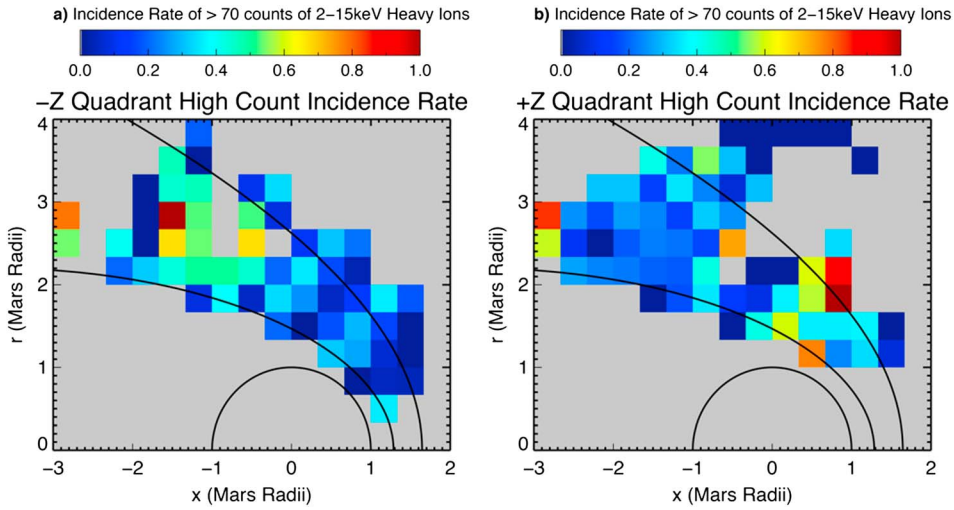

Figure 7. Incidence rate of high counts in the (left) $-Z_{MSE}$ quadrant and in the (right) $+Z_{MSE}$ quadrant in cylindrical coordinates. The color of each spatial bin denotes the likelihood of measurements taken there having greater than 70 counts of 2–15 keV heavy ions. Spatial bins for which there were not at least 10 measurements in this quadrant appear in grey.

each spatial bin in the $+E_{SW}$ hemisphere and the corresponding spatial bin in the $-E_{SW}$ hemisphere. Hence, positive values (red) indicate regions with a higher incidence rate of energetic heavy ion events in the $+E_{SW}$ hemisphere and negative values (blue) indicate regions where it was more common to observe energetic heavy ions in the $-E_{SW}$ hemisphere. Spatial bins for which at least one hemisphere had fewer than 10 measurements appear grey. To see maps with fuller coverage of every figure for which minimum measurement requirements were set (Figures 4, 5, and 7), see the supporting figures to this work, which include reproductions of these maps that color every spatial bin with at least one measurement. Both on the dayside and in the terminator region, there is a higher incidence rate in the $+E_{SW}$ hemisphere. In a few locations on the nightside there were actually more incidences of high counts in the $-E_{SW}$ hemisphere; however, these $-E_{SW}$ hemisphere enhancements may not be significant, as will be seen in further analysis below.

We require that the integrated counts detected during 129 s are at least 70. This is not an arbitrary cutoff. Figure 6 shows that the distribution of count rates is bimodal, with most of the 8,000 data packets having either less than 40 counts or between ~70 and 130 counts. The times with fewer than 40 counts are times when the heavy ions measured are scattered across the IMA's 16 by 16 field of view. Data packets falling within the second peak also exhibit this scattered signature, but in addition to the scattered signature, these times see a large number of entering IMA from the same look direction, more than from all other look directions combined. A plot of ion flight direction over the course of six consecutive IMA sweeps has been included in Figure S7 to provide an understanding of typical differences between the two distinct peaks in Figure 6. The first peak represents the typical background level of counts, whereas the second peak tends to correspond to times when a focused of beam with significant counts is present. Therefore, when we talk about the incidence rate of "high" counts of 2–15 keV heavy ions, this may also be thought of as the occurrence frequency of heavy ion beams.

A close inspection of Figure 4 reveals that the dayside region of high incidence of >70 counts (seen in yellow and orange in Figure 4b) may be caused primarily by a projection of measurements taken in the $-Y_{MSE}$ sector (Figure 4a) onto the plane of the plot in Figure 4b. What would happen if we prevented these Y_{MSE} sector measurements from impacting results? To answer this question, in addition to comparing the $+E_{SW}$ and $-E_{SW}$ hemispheres, data were sorted into quadrants, with all measurements taken within ±45° of the direction of E_{SW} categorized as belonging to the $+Z_{MSE}$ quadrant, and all measurements taken more than 135° from the direction of E_{SW} falling into the $-Z_{MSE}$ quadrant. Figure 7 shows the incidence rate of high counts in cylindrical coordinates, with Figure 7a showing the $-Z_{MSE}$ quadrant, or quarter-cylinder, and Figure 7b showing the $+Z_{MSE}$ quadrant. The use of a cylindrical coordinate system here makes it more readily apparent than in previous figures that all of the data are confined to locations beyond the Vignes et al. (2000) IMB location, which is shown on the plot. The results look similar to what was seen when comparing hemispheres. On

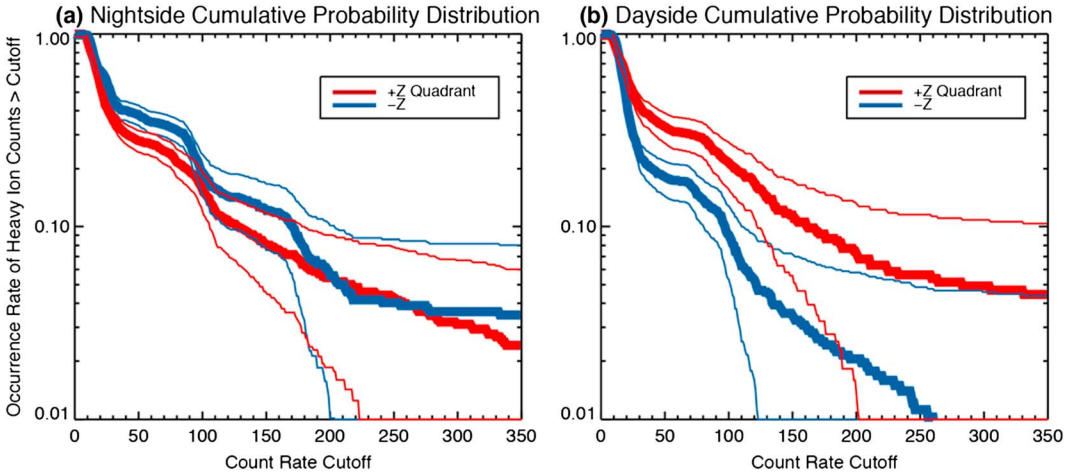

Figure 8. Cumulative probability distributions of 2–15 keV heavy ions outside the Mars IMB for the (a) nightside and (b) dayside. The red line shows the probability distribution of the $+Z_{MSE}$ quadrant (quarter-cylinder), and the blue line shows the distribution for the $-Z_{MSE}$ quadrant. The vertical axis shows the proportion of data packets for which the count rate exceeded the cutoff indicated on the horizontal axis. The higher the cutoff, the smaller the proportion of data packets exceeding this threshold, causing the lines to slope down monatonically. The thin lines are 90% confidence windows based on counting statistics.

the dayside, MEX was more likely to see high counts when in the $+Z_{MSE}$ quadrant, while on the nightside it appears that MEX was more likely to see a high count rate the $-Z_{MSE}$ quadrant.

To quantify the differences between quadrants, cumulative probability distributions were created to show what proportion of the time the count rate exceeded any given value. Figure 8 presents such cumulative probability distributions, comparing the $+Z_{MSE}$ and $-Z_{MSE}$ quadrants on the nightside (Figure 8a) and on the dayside (Figure 8b). The thicker lines show the occurrence frequency, or incidence rate, of high-count events versus the range of possible count limits that might have been used to define what is meant by "high counts." The portions of the cumulative probability distribution with steep slopes correspond to count rates that occur more frequently, as seen in the histogram (Figure 6). The flat (horizontal) portions of the probability distribution correspond to low points in the histogram. The thin lines in Figure 8 represent 90% confidence windows. As the count rate cutoff increases, the number of data packets with counts exceeding this cutoff falls rapidly, greatly decreasing the degree of certainty surrounding this cutoff's occurrence frequency, leading to wider confidence windows. As expected, Figure 8b demonstrates that on the dayside, the $+Z_{MSE}$ quadrant saw more heavy energetic ions than did the $-Z_{MSE}$ quadrant. Figure 8a reveals that narrowing our focus to opposite quadrants retains the unexpected reverse asymmetry seen on the nightside, with the nightside seeing a slight preference for high count rates in $-Z_{MSE}$ quadrant rather than $+Z_{MSE}$ quadrant, but the overlapping confidence windows suggest that this might be due to a limited amount of data. The confidence windows for the dayside Figure 8 do not overlap until reaching extremely rare high rates, indicating that the dayside asymmetry, more heavy ions in the direction of E_{SW}, is much more certain. It should be noted that the confidence windows only represent the uncertainty due to counting statistics. In other words, if we were 100% certain that all estimates of the IMF direction were correct, *and* 100% certain that all oxygen actually present was detected and that there were no false oxygen counts, *and* if spatial coverage were even (no patches without data), then we could say with 90% confidence that the true probability distribution lies within this confidence window. These confidence windows allow us to see that for count rates that are sufficiently rare (count rates greater than about 200), the uncertainty due to the small amount of data becomes quite large. An alternative method of displaying most of this same information, noncumulative probability distributions, appears in Figure S3.

An additional approach to presenting the E_{SW}-based asymmetry seen by MEX is shown in Figure 9, where a cylindrical coordinate system is employed in conjunction with units of particle flux. As in Figure 7, the coordinate system in Figure 9 divides the space around Mars into $+Z_{MSE}$ and $-Z_{MSE}$ quadrants, with data integrated along curves of constant cylindrical radius. The colorscale now shows particle flux (rather than

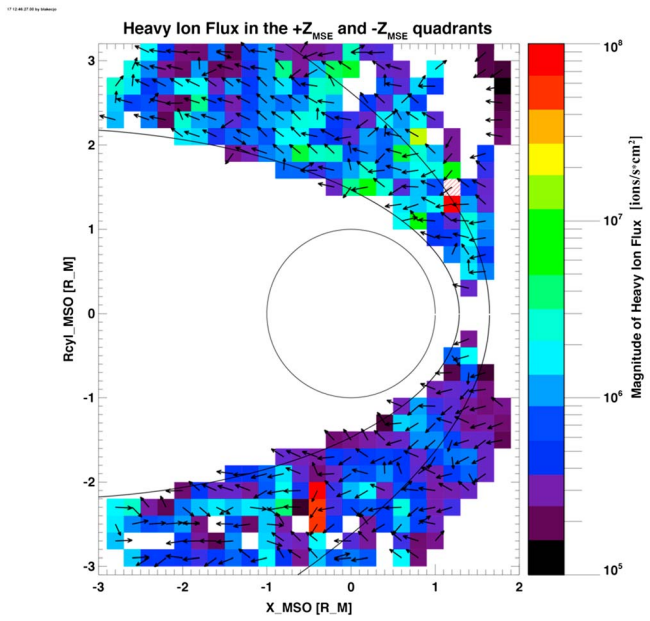

Figure 9. 2–15 keV heavy ion particle flux magnitude (color) and direction (arrows). The coordinate system used is the equivalent of two quarter-cylinders, where data have been sorted into $+Z_{MSE}$ (top half) and $-Z_{MSE}$ (bottom half) quadrants before integration along curves of constant radius$_{cyl}$.

counts), with arrows indicating direction and color indicating magnitude. Fluxes are integrated over all look directions, showing omnidirectional flux with units of ions per second per cm^2. The direction arrows show an average of two components of the flow for all data packets in that spatial bin, averaging the radial component and the longitudinal component, while ignoring the azimuthal velocity component in this calculation. The method used to calculate these fluxes is the same as that used in Nilsson et al. (2011). Binning by energy, spatial location, and flight angle in cylindrical coordinates is used, with average flux calculated separately for each bin so that uneven sampling of flight direction does not influence results. A full description of this technique can be found in Fraenz et al. (2015). The arrows show a general motion away from subsolar location and an upward-outward motion in the $+E_{SW}$ nightside. Other locations have seemingly random flow directions. This is addressed in section 4.

The color bar in Figure 9 has been tweaked to highlight the hemispheric asymmetry, but just as was done in Figure 5, a difference plot has been provided to make comparison between hemispheres even easier. In Figure 10, which uses the same coordinate system as Figure 9, flux values from the $-E_{SW}$ hemisphere have been subtracted from flux values from the corresponding spatial bin in the $+E_{SW}$ cylindrical hemisphere. The red spatial bins indicate regions in which the $+E_{SW}$ hemisphere experienced higher mean particle fluxes of heavy ions than did the $-E_{SW}$ hemisphere, while the blue colors represent regions in which the mean fluxes in the $-E_{SW}$ hemisphere were larger. The large dayside region where red dominates indicates higher fluxes of heavy energetic ions in the $+E_{SW}$ hemisphere located where hybrid and particle tracking models have predicted the energetic plume to be (e.g., Fang et al., 2008). The hemispheres seem far more similar on the nightside, perhaps even with an indication of slightly higher fluxes measured by MEX in the near-terminator nightside, as seen in Figure 5.

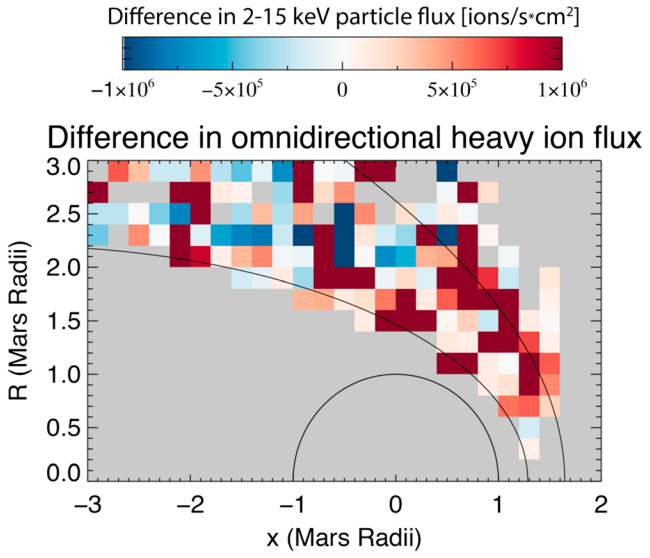

Figure 10. Difference in magnitude of 2–15 keV heavy ion particle flux. The coordinate system is the same as that used for Figure 9. Flux values from the $-Z_{SW}$ quadrant have been subtracted from flux values from the corresponding location in the $+Z_{SW}$ quadrant, so that negative values (blue) represent locations where the mean flux was greater in the $-Z_{SW}$ quadrant, while positive values (red) represent locations where there was greater flux in the $+Z_{SW}$ quadrant.

4. Discussion

The results presented above indicate that on the dayside there is a clear $+E_{SW}$ preference for observation of 2–15 keV heavy ions. On the nightside, this was not seen. This is in general agreement with the numerical models that predict a focused energetic plume of planetary ions escaping from Mars in the direction of the solar wind convective electric field.

It is interesting to note that Liemohn et al. (2014), who conducted a similar survey of energetic (2–5 keV) planetary ions (specifically, O^+) beyond the IMB (from the 2004–2006 MEX-MGS overlap interval), did not find this systematic occurrence rate and flow pattern in favor of $+E_{SW}$. This apparent discrepancy can be readily explained, however, by taking into account the differences between the two methodologies of the surveys. First, the selection criterion with respect to E_{SW} is different. The former study used a window of ±30 min around any of the $\cup_{IMF}$ values from MGS, whereas the present study only uses the MEX ion data if the clock angle is "steady," as defined above. Second, the criterion with respect to what is considered "high counts" is different. The former study chose a cutoff of 200 counts to be classified as a significant observation of planetary ions, while the present study uses the more defensible value based on the bimodal distribution of count rates (i.e., 70). Third, the criterion with respect to number of data packets in the presentation of the incidence rates is different. The former study has no lower threshold for including the value for a particular spatial bin, while the present study requires a minimum of 20 measurements in a spatial bin before it is shown in Figure 4. Fourth and finally, the plot-style

presentation of the results is made differently. The former study only considered the *X*-integrated *Y*-*Z* plane format (MSE coordinates as viewed from the Sun), while the present study uses a variety of formats. All of these small but important distinctions between the methodologies lead to the present study producing more definitive answers regarding the characteristics of energetic planetary ions beyond the IMB at Mars.

Regarding velocities shown in Figure 9, they do not consistently match what would be expected from high energy pickup ions accelerated by the convection electric field, but this does not necessarily mean there is a need to search for alternative acceleration mechanisms. The fluxes seen in Figure 9 are directed more downtail (less radially outward) than is typically associated with the energetic plume, but this is due at least in part to the cylindrical coordinate system used, in which the radial component incorporates the Y_{MSE} velocity as well as the Z_{MSE} velocity. Still, the velocity vectors shown are more erratic than those appearing in work using the same method but looking at lower energies (see Fraenz et al., 2015). There are at least three possible explanations for this. First, it is possible that some of the heavy ions in the 2–15 keV energy range were accelerated by a process other than motional electric field, causing them not to follow the bulk plume flow direction. Second, there was concern that even though a concerted effort has been made to avoid ghost H^+ counts, the number of ions at such high energies is so low that even a very small amount of H^+ contamination could impact results in some spatial bins. Spot-checking revealed proton contamination to be rare but not nonexistent in the mass and energy ranges used in this study. The global picture should be largely unaffected. Finally, velocity vectors are also affected by the large uncertainty in the angle of rotation to achieve MSE coordinates for each data packet, which leads to incorrect binning. It is likely that many of the values creating the vectors in one quadrant would actually be in another quadrant if the IMF proxies were perfect. This will lead to, for example, measurements from Y_{MSE} quadrants sneaking into the Z_{MSE} quadrant and making the mean flow direction less radial than what is expected for the energetic plume.

The reverse-asymmetry seen on the nightside, in which 2–15 keV heavy ions are seen more in the $-E_{SW}$ direction than in the $+E_{SW}$ direction (Figures 5, 10, and 8a), might be explained by arguing that many of the ions measured are in fact plume particles moving more radially outward than the averaged flux vectors indicate, leaving a relative void of energetic heavy ions immediately antisunward of the main plume of radially directed ions. Keeping in mind that Figure 3 shows that there is little data from the $-E_{SW}$ nightside; however, a more mundane possibility is that the apparent reversal in E_{SW} asymmetry in portions of the nightside is a product of low counting statistics (recall the overlapping error bars in Figure 8a). It is important to note that Dong et al. (2015), which was able to directly measure the direction E_{SW} with MAVEN's magnetometer when MAVEN was upstream of the bow shock, found no such reverse asymmetry on the nightside. Instead, across all values of X_{MSE} examined, Dong et al. (2015) saw greater fluxes of O^+ in the $+E_{SW}$ hemisphere. This suggests that the reverse asymmetry seen here is due to a combination of low counting statistics and uncertainty in the direction of E_{SW}.

The primary uncertainty in this study is the precise direction of the upstream IMF. The exclusion of times when the draping direction of the IMF was unsteady has played a role in revealing a clearer global asymmetry than was seen in Liemohn et al. (2014), but the results presented here still rely on the assumption that the magnetic field at 400 km altitude has the same clock angle as the upstream IMF. It is known that this simplified model of field line draping is an idealization of the actual picture. Brain et al. (2006) found hints of "weathervaning" (a bending of field lines associated with unequal mass-loading along a magnetic flux tube) of the draped field in MGS magnetometer data as well as indications that the toward and away sectors of the solar wind do not result in draping configurations that perfectly mirror each other. Luhmann et al. (2015) presented comparisons of the MGS draping angle with MHD results, finding some agreement but also noticeable differences due to weathervaning and crustal field influences. Xu et al. (2017) used pitch angle measurements from MAVEN's Solar Wind Electron Analyzer to examine magnetic connectivity and found that in the 400–600 km range, at the latitude range used for the draping proxy adopted in the present study, MAVEN saw either closed or open field lines more often than draped field lines (Xu et al.; Figures 8–10). This suggests that the strong clustering of estimates of E_{SW} shown in Figure 2 may be at least partially due to MGS at 400 km, 50–60° latitude, having frequently measured field lines connected to the electron exobase, which may not correspond to draped IMF. The large uncertainty in upstream IMF angle, together with the fact that the clustering of values in Figure 2 suggests that errors in the draping proxy are in part systematic, have inspired the planning of a project in which we will attempt to create a more reliable draping proxy that

could be used to study the entire time period during which MGS was at its 400 km mapping orbit. For the task of identifying hemispheric or quarter-cylinder resolution asymmetries, our analysis has convinced us that the Brain proxy is sufficient, allowing us to establish that the MEX ion data, used carefully and in conjunction with MGS, can be used to observe the planetary ion energetic plume statistically.

Limitations of the IMA instrument have also affected the results reported here. First, the IMA duty is such that it is often inactive when MEX is at very high altitudes, where these E_{SW}-accelerated ions are most likely to be seen. Second, IMA was mounted on the spacecraft, in part, "to co-aligned the central plane of the IMA field of view with the ecliptic plane when the spacecraft is in the Earth pointing mode" (Barabash et al., 2006). An unfortunate effect of this alignment is that when the IMF is in the ecliptic plane, E_{SW} is aligned with one of IMA's field of view holes. Measurements in Dong et al. (2017) depict energetic plume flow directions that such a field of view hole would be expected to miss, and a specific example of this can be seen in the case study of the plume performed by Liemohn et al. (2014) in which very strong ion beam is seen at the furthest extent of IMA's elevation angle, suggesting part of this population may have been missed by IMA. The distribution of E_{SW} shown in Figure 2 shows that much or even most of the time the IMF was estimated to not be in the ecliptic plane. However, since the field of view hole issue is expected to be worst for what is in general the most common IMF orientation, surveys of the energetic plume using MEX cannot hope to obtain realistic estimates of plume fluxes or escape rates.

An additional uncertainty may stem from any seasonal variations of the energetic plume or of IMF draping around Mars. The period of time covered by this study is only slightly longer than one Mars year, too short of an interval to identify seasonal patterns or to guarantee that effects of seasonal variations are completely washed out in the statistics. Using MAVEN's STATIC instrument was found by Dong et al. (2017), where plume escape fluxes did not appear to vary significantly with EUV flux. However, of the two time periods considered by Dong et al., the period closer to the maximum of solar cycle 24 (and hence the time period from which their larger EUV values were drawn) was 11 November 2014 to 19 March 2015, which also happens to be a period that straddled Mars' northern winter solstice. It has been found that during southern summer conditions such as this, the strong crustal field region raises the altitude of the IMB across the entire dayside (Brain et al., 2005). Thus, the unexpected result in Dong et al. (2017), that increased EUV did not correlate with increased plume fluxes, may be due to the period of higher EUV coinciding with a period of high IMB. A higher IMB would mean that fewer ions were born outside of this raised IMB, and ions born inside the IMB would be less likely to make it out into the magnetosheath where E_{SW} is strong, effects which would tend to counteract the increased scale heights and increased production rates of a high EUV time period. Such possible seasonal effects should also exist in the present study. The time period we used included two northern summers but only one northern winter.

Given the broader communal goal of developing estimates of atmospheric loss on geological timescales, the question of how plume escape changes with key time-varying parameters is deeply important. MAVEN observations have shown the plume as well as the role of the solar wind convection electric field in creating the plume (Brain et al., 2015; Dong et al., 2017). However, exploring the time variation of plume escape with limited amounts of data is very difficult. The difficulties associated with limited data have been highlighted in the previous paragraph's discussion of Dong et al. (2017), where it was noted that the period of high EUV flux also happened to correspond to a season that may counteract the influence of increased EUV. With MAVEN likely to begin prioritizing its role as a relay between Earth and assets on the Martian surface only a fraction of a solar cycle after its Mars orbital insertion, the importance of expanding the periods of time open to study is being made even more clear. As the only statistical study using IMA data to identify characteristics of this plume population by focusing specifically on the relevant locations and particle energies, we believe that this study is a first step toward opening a time period unseen by MAVEN to exploration of the plume and its variability.

We have shown that despite the fact that the MEX mission was not designed to prioritize study of the energetic plume population, MEX IMA can and does see a statistical plume. The next step is to examine how the plume, as seen by IMA, varies with parameters such as EUV flux, crustal field positioning, and solar wind parameters. This examination of drivers, however, is complicated by our finding that these same drivers of plume escape rates can be shown to influence the IMF clock angle proxy used in the present study. This could lead to a result in which we are uncertain of whether a driver's correlation with a perceived stronger plume is truly

due to increased plume loss or whether the actual correlation is between the driver and better estimates of the $+E_{SW}$ direction. Untangling these effects is beyond the scope of the present study. It is our hope that these exercises may be more fruitful after completion of a project currently under way to improve the IMF draping proxy.

5. Conclusions

This work focused on global asymmetries in the heavy ion population outside of the Martian IMB in the 2–15 keV energy range as seen by ion mass spectrometer IMA on Mars Express. A new methodology was implemented to isolate the energetic heavy ion signature in the MEX IMA data set, avoiding the ubiquitous solar wind proton contamination which usually obscures this measurement outside of the IMB. The time period during which MGS magnetometer data was available was trimmed down to times when the clock angle of the IMF was steady over a period of several hours. Using MGS estimates for the direction of the upstream IMF direction, MEX ion data were rotated into MSE coordinates.

We conclude that while the overall picture of flight direction remains unclear, there is a statistical asymmetry based on E_{SW} in the high-altitude energetic heavy ion population, as has been discussed previously in case studies (Dubinin et al., 2011; Edberg et al., 2009; Liemohn et al., 2014) and in surveys performed using MAVEN data (Brain et al., 2015; Dong et al., 2015, 2017). Unexpectedly, on the nightside it was in the $-E_{SW}$ hemisphere where more 2–15 keV heavy ions were detected, but this is likely attributable to insufficient counting statistics in this region. The difference between the $+E_{SW}$ quadrant and the $-E_{SW}$ quadrant was significant on the dayside, which is consistent with kinetic models showing a somewhat narrow plume feature of heavy ions accelerated in the direction of E_{SW}.

Acknowledgments
The authors thank NASA and NSF for supporting this work, particularly under NASA grants NNX11AD80G, NNX13AG26G, and NNX14AH19G and NSF grant AST-0908311. The ion data are available at the ASPERA-3 website at the Swedish Institute for Space Physics, http://aspera-3.irf.se/thedata and have been processed using the CCATi software package written in IDL. The draping proxy developed by Dave Brain is available at http://sprg.ssl.berkeley.edu/~brain/proxies.html. The authors would like to thank the reviewers for their valuable comments and suggestions toward the final version of the manuscript.

References

Barabash, S., Dubinin, E., Pisarenko, N., Lundin, R., & Russell, C. T. (1991). Picked-up protons near Mars-PHOBOS observations. *Geophysical Research Letters*, *18*(10), 1805–1808. https://doi.org/10.1029/91GL02082

Barabash, S., Lundin, R., Andersson, H., Gimholt, J., Holmstrom, M., Norberg, O., … Bochsler, P. (2004). ASPERA-3: Analyser of Space Plasmas and Energetic Ions for Mars Express. In *Mars Express: The Scientific Payload* (pp. 121–139). Noordwijk, Netherlands: SP-1240, ESA Publications Division.

Barabash, S., Lundin, R., Andersson, H., Brinkfeldt, K., Grigoriev, A., Gunell, H., … Thocaven, J.-J. (2006). The Analyzer of Space Plasmas and Energetic Atoms (ASPERA-3) for the Mars Express mission. *Space Science Reviews*, *126*, 113–164.

Barabash, S., Fedorov, A., Lundin, R., & Sauvaud, J.-A. (2007). Martian atmospheric erosion rates. *Science*, *315*(5811), 501–503. https://doi.org/10.1126/science.1134358

Boesswetter, A., Bagdonat, T., Motschmann, U., & Sauer, K. (2004). Plasma boundaries at Mars: A 3-D simulation study. *Annales de Geophysique*, *22*(12), 4363–4379. https://doi.org/10.5194/angeo-22-4363-2004

Brain, D. A., Halekas, J. S., Lillis, R., Mitchell, D. L., Lin, R. P., & Crider, D. H. (2005). Variability of the altitude of the Martian sheath. *Geophysical Research Letters*, *32*, L18203. https://doi.org/10.1029/2005GL023126

Brain, D. A., Mitchell, D. L., & Halekas, J. S. (2006). The magnetic field draping direction at Mars from April 1999 through August 2004. *Icarus*, *182*(2), 464–473. https://doi.org/10.1016/j.icarus.2005.09.023

Brain, D. A., McFadden, J. P., Halekas, J. S., Connerney, J. E. P., Bougher, S. W., Curry, S., … Seki, K. (2015). The spatial distribution of planetary ion fluxes near Mars observed by MAVEN. *Geophysical Research Letters*, *42*, 9142–9148. https://doi.org/10.1002/2015GL065293

Carlsson, E., Brain, D., Luhmann, J., Barabash, S., Grigoriev, A., Nilsson, H., & Lundin, R. (2008). Influence of IMF draping direction and crustal magnetic field location on Martian ion beams. *Planetary and Space Science*, *56*(6), 861–867. https://doi.org/10.1016/j.pss.2007.12.016

Curry, S. M., Liemohn, M. W., Fang, X., Ma, Y., Nagy, A. F., & Espley, J. (2013). The influence of production mechanisms on pickup ion loss at Mars. *Journal of Geophysical Research: Space Physics*, *118*, 554–569. https://doi.org/10.1029/2012JA017665

Dieval, C., Morgan, D. D., Nemec, F., & Gurnett, D. A. (2014). MARSIS observations of the Martian nightside ionosphere dependence on solar wind conditions. *Journal of Geophysical Research: Space Physics*, *119*, 4077–4093. https://doi.org/10.1002/2014JA019788

Dong, Y., Fang, X., Brain, D. A., McFadden, J. P., Halekas, J. S., Connerney, J. E., … Jakosky, B. M. (2015). Strong plume fluxes at Mars observed by MAVEN: An important planetary ion escape channel. *Geophysical Research Letters*, *42*, 8942–8950. https://doi.org/10.1002/2015GL065346

Dong, Y., Fang, X., Brain, D. A., McFadden, J. P., Halekas, J. S., Connerney, J. E. P., … Jakosky, B. M. (2017). Seasonal variability of Martian ion escape through the plume and tail from MAVEN observations. *Journal of Geophysical Research: Space Physics*, *122*, 4009–4022. https://doi.org/10.1002/2016JA023517

Dubinin, E. M., Sauer, K., Lundin, R., Baumgärtel, K., & Bogdanov, A. (1996). Structuring of the transition region (plasma mantle) of the Martian magnetosphere. *Geophysical Research Letters*, *23*(7), 785–788.

Dubinin, E., Fränz, M., Woch, J., Roussos, E., Barabash, S., Lundin, R., … Acuña, M. (2006). Plasma morphology at Mars. Aspera-3 observations. *Space Science Reviews*, *126*(1-4), 209–238. https://doi.org/10.1007/s11214-006-9039-4

Dubinin, E., Fränz, M., Woch, J., Roussos, E., Barabash, S., Lundin, R., … Acuña, M. (2008). Plasma morphology at Mars: ASPERA-3 observations. *Space Science Reviews*, *126*(1-4), 209–238. https://doi.org/10.1007/s11214-006-9039-4

Dubinin, E., Fraenz, M., Fedorov, A., Lundin, R., Edberg, N., Duru, F., & Vaisberg, O. (2011). Ion energization and escape on Mars and Venus. *Space Science Reviews*, *162*(1-4), 173–211. https://doi.org/10.1007/s11214-011-9831-7

Edberg, N. J. T., Auster, U., Barabash, S., Bößwetter, A., Brain, D. A., Burch, J. L., … Trotignon, J. G. (2009). Rosetta and Mars Express observations of the influence of high solar wind pressure on the Martian plasma environment. *Annales de Geophysique*, *27*(12), 4533–4545. https://doi.org/10.5194/angeo-27-4533-2009

Fang, X., Liemohn, M. W., Nagy, A. F., Ma, Y., De Zeeuw, D. L., Kozyra, J. U., & Zurbuchen, T. (2008). Pickup oxygen ion distribution around Mars. *Journal of Geophysical Research*, *113*, A02210. https://doi.org/10.1029/2007JA012736

Fedorov, A., Budnik, E., Sauvaud, J. A., Mazelle, C., Barabash, S., Lundin, R., … Dierker, C. (2006). Structure of the Martian wake. *Icarus*, *182*(2), 329–336. https://doi.org/10.1016/j.icarus.2005.09.021

Fedorov, A., Ferrier, C., Sauvaud, J. A., Barabash, S., Zhang, T. L., Mazelle, C., … Bochsler, P. (2008). Comparative analysis of Venus and Mars magnetotails. *Planetary and Space Science*, *56*(6), 812–817. https://doi.org/10.1016/j.pss.2007.12.012

Fraenz, M., Dubinin, E., Andrews, D., Barabash, S., Nilsson, H., & Fedorov, A. (2015). Cold ion escape from the Martian ionosphere. *Planetary and Space Science*, *119*, 92–102. https://doi.org/10.1016/j.pss.2015.07.012

Harnett, E. M., & Winglee, R. M. (2006). Three-dimensional multifluid simulations of ionospheric loss at Mars from nominal solar wind conditions to magnetic cloud events. *Journal of Geophysical Research*, *111*, A09213. https://doi.org/10.1029/2006JA011724

Kallio, E., & Koskinen, H. (1999). A test particle simulation of the motion of oxygen ions and the solar wind protons. *Journal of Geophysical Research*, *104*(A1), 557–579. https://doi.org/10.1029/1998JA900043

Kallio, E., Koskinen, H., Barabash, S., Nairn, C. M. C., & Schwingenschuh, K. (1995). Oxygen outflow in the Martian magnetotail. *Geophysical Research Letters*, *22*(18), 2449–2452. https://doi.org/10.1029/95GL02474

Kallio, E., Fedorov, A., Barabash, S., Janhunen, R., Koskinen, H., Schmidt, W., … Sharber, J. R. (2006). Energisation of O+ and O2+ ions at Mars: An analysis of a 3-D quasi-neutral hybrid model simulation. *Space Science Reviews*, *126*, 39–62.

Liemohn, M. W., Ma, Y., Frahm, R. A., Fang, X., Kozyra, J. U., Nagy, A. F., … Lundin, R. (2007). Mars global MHD predictions of magnetic connectivity between the dayside ionosphere and the magnetospheric flanks. *Space Science Reviews*, *126*(1-4), 63–76. https://doi.org/10.1007/s11214-006-9116-8

Liemohn, M. W., Curry, S. M., Fang, X., & Ma, Y. (2013). Comparison of high-altitude production and ionospheric outflow contributions to O^+ loss at Mars. *Journal of Geophysical Research: Space Physics*, *118*, 4093–4107. https://doi.org/10.1002/jgra.50388

Liemohn, M. W., Johnson, B. C., Fränz, M., & Barabash, S. (2014). Mars Express observations of high altitude planetary ion beams and their relation to the "energetic plume" loss channel. *Journal of Geophysical Research*, *119*, 9702–9713. https://doi.org/10.1002/2014JA019994

Luhmann, J. G., & Schwingenschuh, K. (1990). A model of the energetic ion environment of Mars. *Journal of Geophysical Research*, *95*(A2), 939–945. https://doi.org/10.1029/JA095iA02p00939

Luhmann, J. G., Ma, Y.-J., Brain, D. A., Ulusen, D., Lillis, R. J., Halekas, J. S., & Espley, J. R. (2015). Solar wind interaction effects on the magnetic fields around Mars: Consequences for interplanetary and crustal field measurements. *Planetary and Space Science*, *117*, 15–23. https://doi.org/10.1016/j.pss.2015.05.004

Lundin, R., & Dubinin, E. M. (1992). Phobos-2 results on the ionospheric plasma escape from Mars. *Advances in Space Research*, *12*(9), 255–263. https://doi.org/10.1016/0273-1177(92)90338-X

Lundin, R., Barabash, S., Andersson, H., Holmström, M., Grigoriev, A., Yamauchi, M., … Bochsler, P. (2004). Solar wind-induced atmospheric erosion at Mars: First results from ASPREA-3 on Mars Express. *Science*, *305*, 1993–1936.

Lundin, R., Barabash, S., Holmström, M., Nilsson, H., Yamauchi, M., Fraenz, M., & Dubinin, E. M. (2008). A comet-like escape of ionospheric plasma from Mars. *Geophysical Research Letters*, *35*, L18203. https://doi.org/10.1029/2008GL034811

Lundin, R., Barabash, S., Yamauchi, M., Nilsson, H., & Brain, D. (2011). On the relation between plasma escape and the Martian crustal magnetic field. *Geophysical Research Letters*, *38*, L02102. https://doi.org/10.1029/2010GL046019

Modolo, R., Chanteur, G. M., Dubinin, E., & Matthews, A. P. (2005). Influence of the solar EUV flux on the Martian plasma environment. *Annales de Geophysique*, *23*(2), 433–444. https://doi.org/10.5194/angeo-23-433-2005

Najib, D., Nagy, A. F., Tth, G., & Ma, Y. (2011). Three-dimensional, multifluid, high spatial resolution mhd model studies of the solar wind interaction with mars. *Journal of Geophysical Research*, *116*, A05204. https://doi.org/10.1029/2010JA016272

Nilsson, H., Edberg, N. J. T., Stenberg, G., Barabash, S., Holmstrm, M., Futaana, Y., … Fedorov, A. (2011). Heavy ion escape from Mars, influence from solar wind conditions and crustal magnetic fields. *Icarus*, *215*(2), 475–484. https://doi.org/10.1016/j.icarus.2011.08.003

Nilsson, H., Stenberg, G., Futaana, S., Holmstrom, M., Barabash, S., Lundin, R., … Fedorov, A. (2012). Ion distributions in the vicinity of Mars: Signatures of heating and acceleration processes. *Earth, Planets and Space*, *64*(2), 135–148. https://doi.org/10.5047/eps.2011.04.011

Vignes, D., Mazelle, C., Rme, H., Acufia, M. H., Connerney, J. E. P., Mitchell, D. L., … Univer-, R. (2000). Shapes of the bow shock and the magnetic pile-up boundary from the observations of the MAG/ER experiment onboard Mars Global Surveyor. *Geophysical Research Letters*, *27*(1), 49–52. https://doi.org/10.1029/1999GL010703

Wang, X. D., Barabash, S., Futaana, Y., Grigoriev, A., & Wurz, P. (2013). Directionality and variability of energetic neutral hydrogen fluxes observed by Mars Express. *Journal of Geophysical Research: Space Physics*, *118*, 7635–7642. https://doi.org/10.1002/2013JA018876

Xu, S., Mitchell, D., Liemohn, M., Fang, X., Ma, Y., Luhmann, J., … Jakosky, B. (2017). Martian low-altitude magnetic topology deduced from MAVEN/SWEA observations. *Journal of Geophysical Research: Space Physics*, *122*, 1831–1852. https://doi.org/10.1002/2016JA023467